ADVANCED MATERIALS INTERFACES
www.advmatinterfaces.de

Low-Temperature Synthesis of Amorphous Silicon and Its Ball-in-Ball Hollow Nanospheres as High-Performance Anodes for Sodium-Ion Batteries

Fei-Hu Du, Ling Zhang, Yun-Cheng Tang, Shang-Qi Li, Yu Huang, Le Dong, Qianqian Li, Hong Liu, Dong Wang, and Yong Wang**

Silicon is widely developed and deemed as a hopeful anode material for lithium-ion batteries. However, till now there is very little literature devoted to its study for sodium-ion batteries (SIBs). One possible reason is the preparation difficultly of carefully crafted amorphous silicon (a-Si) structures by a facile and low-cost method. Another reason is that a-Si suffers from large volume expansion, slow sodium diffusion kinetics, and poor electrical conductivity. Herein, a new method called as "sodiothermic reduction" is used to prepare a-Si hollow nanospheres at a much lower temperature. Moreover, an a-Si-based composite with yolk-shell structure is designed via atomic layer deposition of alumina, in situ chemical polymerization of pyrrole, and dilute HCl etching. The obtained composite as an anode material for SIBs displays a great initial discharge capacity of 645.6 mAh g^{-1} at 100 mA g^{-1}, superior long steadiness up to 5000 cycles at 800 mA g^{-1}, and preeminent rate capability (646.4, 193.5, 138.6, 105, 77.5 mAh g^{-1} at 100, 400, 800, 1500, 3000 mA g^{-1}, respectively). In situ transmission electron microscopy observation on the structure evolution and finite element analysis of the stress–strain behavior are combined to further prove the merits of the well-designed yolk–shell structure.

1. Introduction

Sodium-ion batteries (SIBs) are expected to be a fascinating replacement to lithium-ion batteries (LIBs) because of the high usability of sodium resources as well as the semblable chemical characteristics of sodium and lithium.[1] However, it is usually more difficult to develop anode materials of SIBs than that of LIBs, attributing to the large radius of the sodium-ion (Na^+ 1.02 Å vs Li^+ 0.76 Å).[2] Silicon, especially possessing crystalline phase, has been widely exploited and thought of as a hopeful anode material for LIBs owing to its unparalleled theoretical capacity, environmentally friendly character, and rich natural resources.[3–5] Unfortunately, crystalline silicon (c-Si) possesses extremely finite sodium storage capability based on first-principle calculations due to the large energy consumption of sodium insertion into c-Si.[6,7] On the contrary, amorphous silicon (a-Si) is capable of holding 0.76 Na atom each Si, the capacity is highly 725 mAh g^{-1} correspondingly.[7] Till now, there is only a little literature dedicated to the study of a-Si as an anode material for SIBs.[8–12] One reason for this is the preparation difficultly of a-Si. Expensive and unstable raw materials such as silicon tetrachloride and complicated devices are usually involved. Moreover, most of these a-Si have no special structures, leading to unsatisfactory Na-storage performance. Silica with a non-toxic, easy to use, and stable chemical property, is abundant in nature. Carbothermic reduction is a common industrial procedure to manufacture solar energy c-Si from quartz sand (natural mineral) in an electric arc furnace described in Equation (1).[13] Since *Nature* published the first report in 2007 on using magnesiothermic reduction to prepare c-Si from diatom frustules (marine plant) according to Equation (2),[14] the method has been extensively applied in the field of LIBs.[4,5,15] Therefore, it will be of great significance to develop a low-temperature facile approach to produce carefully crafted a-Si structures from silica for SIBs.

$$SiO_2 + 2C \xrightarrow{>1900\,^{\circ}C} Si + 2CO \quad (1)$$

$$SiO_2 + 2Mg \xrightarrow{650\,^{\circ}C} Si + 2MgO \quad (2)$$

F. H. Du, L. Zhang, Y. C. Tang, S. Q. Li, H. Liu, Y. Wang
School of Environmental and Chemical Engineering
Shanghai University
99 Shangda Road, Shanghai 200444, P. R. China
E-mail: yongwang@shu.edu.cn

The ORCID identification number(s) for the author(s) of this article can be found under https://doi.org/10.1002/admi.202102158.

DOI: 10.1002/admi.202102158

Y. Huang, Q. Li
Materials Genome Institute
Shanghai University
99 Shangda Road, Shanghai 200444, P. R. China

L. Dong, D. Wang
School of Mechanical Engineering
Shanghai Jiao Tong University
800 Dongchuan Road, Shanghai 200240, P. R. China
E-mail: wang_dong@sjtu.edu.cn

Another major challenge is how to mitigate several problems that originate from a-Si nature, including large volume expansion (≈114%),[7] slow sodium diffusion kinetics (≈7×10^{-10} cm^2 s^{-1})[7] and poor electrical conductivity (≈3×10^{-5} Ω^{-1} cm^{-1}).[16] Recently, yolk-shell structures have been confirmed to be a very valid idea to improve the electrochemical properties of alloy-type anode materials.[17,18] The gap between yolk and shell enables the electroactive material to swell freely without ruining the conducting layer, guaranteeing stable solid electrolyte interface (SEI) film formation. Silica was often used as a sacrificial layer and etched away by HF or NaOH solution to generate void space.[17,18] Nevertheless, electroactive material, especially silicon, could be easily eroded at the same time, causing the decrease of the whole capacity. Furthermore, the depletion of silicon would result in uncontrollable void space. Too large space will make silicon during cycling unable to contact with the outer layer, whereas too small space will lead to outer layer fracture. More recently, atomic layer deposition (ALD) has been served as a technique to evenly and controllably coat alumina on the surface of germanium nanoparticles. Dilute HCl can be used to remove the sacrificial layer to form yolk-shell structure.[19]

Herein, we report a fresh strategy for the fabrication of an amorphous silicon-based composite with yolk-shell structure via low-temperature (450 °C) sodiothermic reduction of silica, ALD of alumina, in situ chemical polymerization of pyrrole, and dilute HCl etching. As a novel anode material for SIBs, the obtained composite demonstrates impressive electrochemical performance. By in situ transmission electron microscopy (TEM) and finite element (FE) analyses, the excellence of the yolk–shell structure in the sodiation course of the composite is studied.

2. Results and Discussion

2.1. Structure and Morphology Characterization

Figure 1a shows the preparation route for the amorphous silicon hollow nanospheres@void@polypyrrole (a-Si@void@PPy) composite. First, mesoporous silica hollow nanospheres ($MHSiO_2$) were prepared according to our previous work.[5] Second, a-Si was generated through the reduction of $MHSiO_2$ by Na at 450 °C under vacuum condition based on Equation (3). Extra care is needed to deal with residual Na when the reaction is finished.

$$xSiO_2 + 4Na \xrightarrow{450^{\circ}C} xSi + 2Na_2O_x, 1 < x < 2 \quad (3)$$

Third, the as-prepared a-Si was coated with alumina as the sacrificial coating layer using ALD. Then the polyvinyl pyrrolidone (PVP) as a soft layer was encapsulated on the surface of the a-Si@Al_2O_3 nanospheres. The polymerization of pyrrole monomers between the area of the a-Si and PVP layer was induced by $FeCl_3$ oxidant, finishing with the appearance of a-Si@Al_2O_3@PPy. Finally, the sacrificial alumina layer was removed by dilute HCl to obtain the a-Si@void@PPy composite.

According to scanning electron microscopy (SEM) and transmission electron microscopy (TEM) results (Figure 1b,e), the average size of the silica nanospheres is ≈630 nm and the shell thickness is ≈85 nm. Nitrogen adsorption-desorption isotherm (Figure S1a, Supporting Information) exhibits that the silica nanospheres possess the typical mesoporous structure properties. The Brunauer–Emmett–Teller (BET) analysis demonstrates that the $MHSiO_2$ has a surface area of ≈ 884 m^2 g^{-1}, while the pore distribution is ≈2.9 nm in diameter from the Barrett–Joyner–Halenda (BJH) method. Through sodiothermic reduction, the color of the powder in the vacuum glass tube changes from white to black (Figure S2, Supporting Information). After further washing with dilute HCl, the color of the silicon becomes earthy yellow (Figure S3, Supporting Information). As shown in **Figure 2**a, the amorphous character of the silicon is indicated using X-ray diffraction (XRD), where no obvious peaks for c-Si are found. The Raman spectra of the silicon (inset of Figure 2b) show that the band centered ≈477 cm^{-1} is a typical feature of amorphous silicon vibration modes, ascribing to transverse optic phonon.[20] As illustrated in the Si 2p XPS spectrum of a-Si, the distinct peak at ≈99.7 eV is corresponding to the bonding of Si-Si (Figure 2c). Moreover, relatively weak peaks at 103.5 and 101.8 eV are attributed to the Si-O interaction.[9] A small number of silicon oxides may be generated on the surface during the exposure of the a-Si to air. SEM and TEM studies (Figure 1c,f) manifest that the shape of the a-Si is consistent with that of the $MHSiO_2$. The pore size distribution of the a-Si is around 7.5 nm with a surface area of ≈315 m^2 g^{-1} (Figure S1b, Supporting Information), but previous research found that the c-Si obtained by magnesiothermic reduction of $MHSiO_2$ has a higher pore size distribution and lower specific surface area.[5] Furthermore, the reaction temperature (450 °C) in this work is lower than that (650 °C) in the literature,[14] facilitating energy saving and reduction of pollution. More importantly, the whole synthesis process was carried out under vacuum or inert atmosphere, avoiding the fire accident. Therefore, sodiothermic reaction is better than magnesiothermic reaction in terms of lower reaction temperature, stronger structural integrity of Si and higher operational safety.

SEM and TEM images (Figure S4, Supporting Information) reveal that the surface of the a-Si is completely and evenly coated with alumina. The XRD result of the a-Si@Al_2O_3 composite evinces that alumina is amorphous in structure, which can easily be etched by dilute HCl. After in situ chemical polymerization of pyrrole and subsequent template removal, the as-obtained a-Si@void@PPy composite has an interesting ball-in-ball morphology, where per a-Si is encapsulated by one hollow PPy nanosphere with the thickness of gap between the a-Si yolk and PPy shell of 36 nm (Figure 1d,g). The composite consists of Si, C, N, and O elements from the energy-dispersive X-ray (EDX) result (Figure 1j). The dark field scanning TEM image and elemental mappings obviously discover an even and continuous coating of PPy throughout the a-Si (Figure 1h,i). After a-Si is completely removed with NaOH aqueous solution, the hollow PPy nanospheres maintain structurally steady (Figure S5, Supporting Information). The XRD pattern of the a-Si@void@PPy composite displays no extra peaks when compared with that of the a-Si, suggesting the amorphous property of the PPy (Figure 2a). Notably, the peak at 23° for the a-Si left

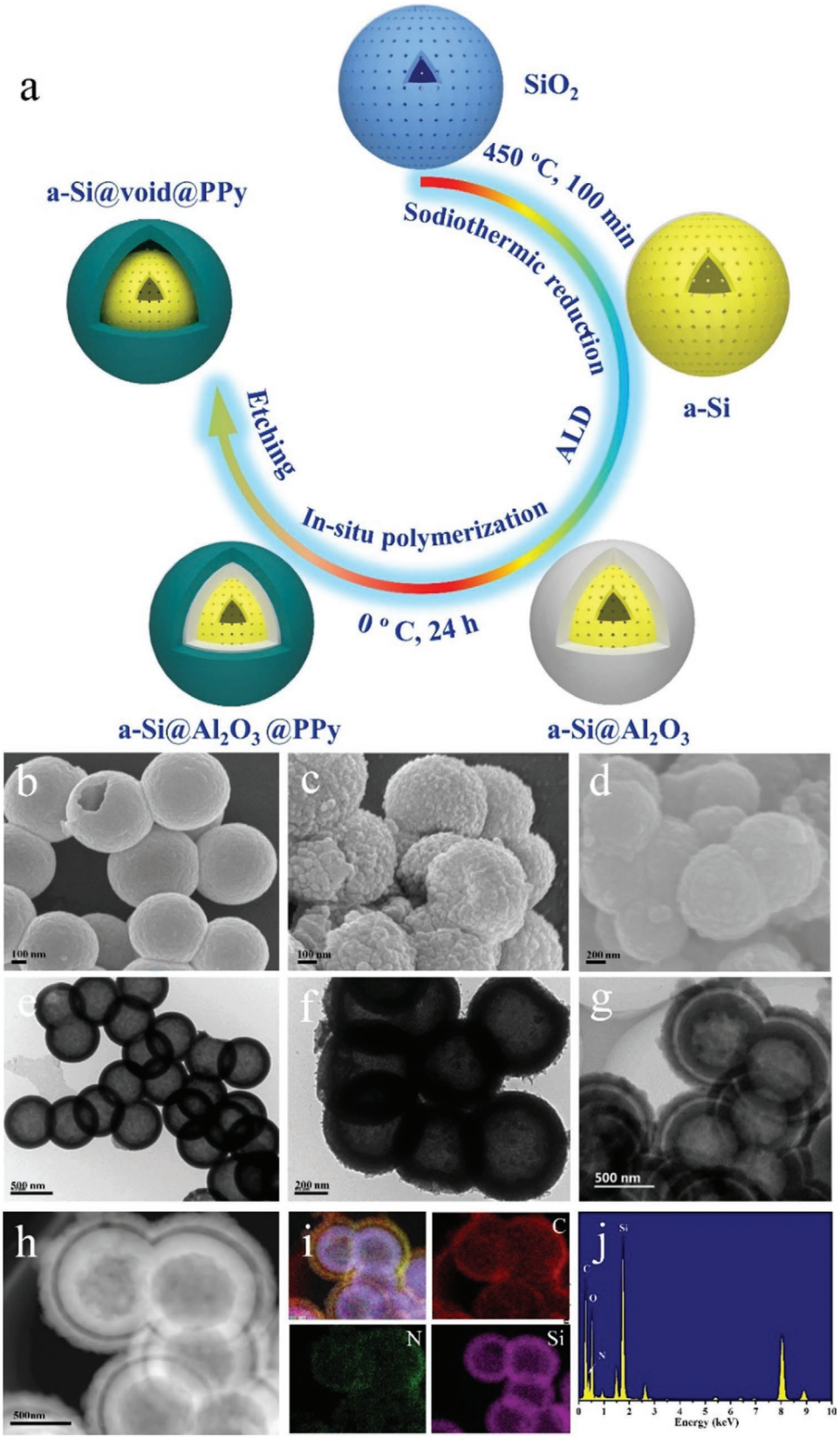

Figure 1. a) Schematic diagram of the synthesis route for an a-Si@void@PPy composite. b–d) SEM images of (b) the $MHSiO_2$, (c) a-Si, and (d) a-Si@void@PPy composite. e–g) TEM images of (e) the $MHSiO_2$, (f) a-Si, and (g) a-Si@void@PPy composite. h) Dark field STEM image of the a-Si@void@PPy composite. i) EDX mappings of C, N, and Si in the a-Si@void@PPy composite. j) EDX spectrum of the a-Si@void@PPy composite.

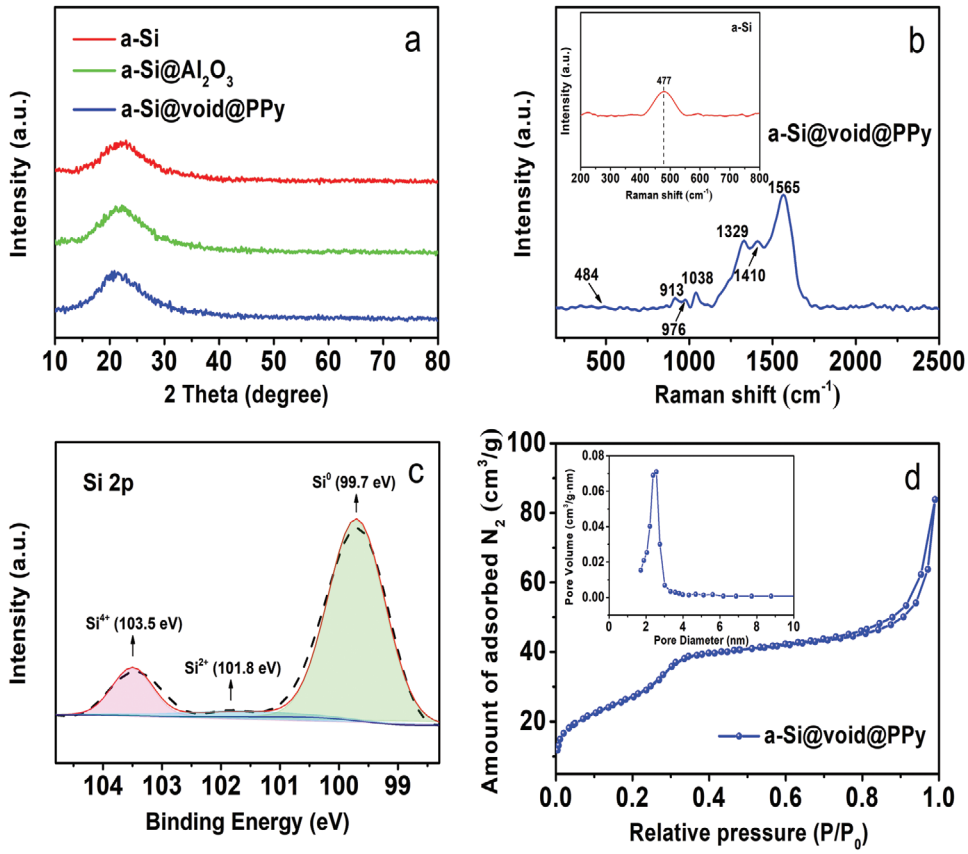

Figure 2. a) XRD patterns of the a-Si@void@PPy composite, a-Si@Al_2O_3 and a-Si. b) Raman spectrum of the a-Si@void@PPy composite and a-Si. c) HR-XPS Si 2p spectra of the a-Si. d) Nitrogen adsorption-desorption isotherms and the corresponding pore size distribution curves (inset) of the a-Si@void@PPy composite.

shifts to ≈21° for the composite, demonstrating that PPy can be uniformly and densely coated on the a-Si surface. The Raman spectra of the a-Si@void@PPy composite show that the peaks between 900 and 1600 cm^{-1} agree well with that of pure PPy from previous study (Figure 2b).[5] It is noteworthy that it is difficult to clearly observe the a-Si Raman peak in the composite, implying that a-Si is completely wrapped by PPy. The pore size of the a-Si@void@PPy composite is ≈5.0 nm with a surface area of 109 m^2 g^{-1} (Figure 2d). The decreased results indicate that the in situ formation of PPy partially fills the pores of the a-Si. The thermogravimetric analysis (TGA) determines that the mass content of a-Si in the composite is ≈84% (Figure S6 and Table S1, Supporting Information).

2.2. Electrochemical Performance

According to cyclic voltammograms (CVs) of the a-Si@void@PPy composite, the irreversible peaks at voltages of ≈1.0 and ≈0.8 V in the initial cathodic scan are found and weaken since the second cycle (**Figure 3**a). These characteristics may be related to surface reactions such as solid electrolyte interphase (SEI) layer generation and reduction of the native oxide film. Remarkably, the cathodic peaks located at ≈0.01 V are ascribed to the Na^+ insertion into the carbon black additive. The electrochemical Na-alloying in a-Si happens from below ≈0.6 V, while de-alloying occurs through a more extensive potential range from above ≈0.7 to ≈1.6 V. Moreover, the anodic peaks appearing at ≈0.11 V turn up from the second cycle, which are attributed to the Na^+ extraction from the carbon black.[8,11] The galvanostatic charge–discharge plots of the a-Si@void@PPy composite in the 0.01–3 V window for the first, second, and 200th cycles at 100 mA g^{-1} are exhibited in Figure 3b. In the initial discharge course, one voltage plateau at ≈1.2 V means the emergence of SEI film and the insertion of Na^+ into a-Si is the explanation for another long sloping lower plateau (<0.6 V). Moreover, the first charge capacity is 251.4 mAh g^{-1} with the first discharge capacity of 645.6 mAh g^{-1}. Wastage of the first reversible capacity is the result of the decomposition of the electrolyte and the parasitic reaction between Na^+ and Si, endowing the surface of the electrode with an SEI film.

The cycling performance of the a-Si@void@PPy electrode is examined at 100 and 800 mA g^{-1} (Figure 3c,e). The electrode exhibits discharge capacities of 217.8 mAh g^{-1} at 100 mA g^{-1} after 200 cycles and 158.2 mAh g^{-1} at 800 mA g^{-1} after 5000 cycles, which amount to 73% and 78% of corresponding that at the second cycle, respectively. Furthermore, Coulombic efficiencies of above 90% are strongly maintained after the 30th cycle at 100 and 800 mA g^{-1}. The cyclic behavior of carbon black and PPy was also examined (Figure S7, Supporting Information),

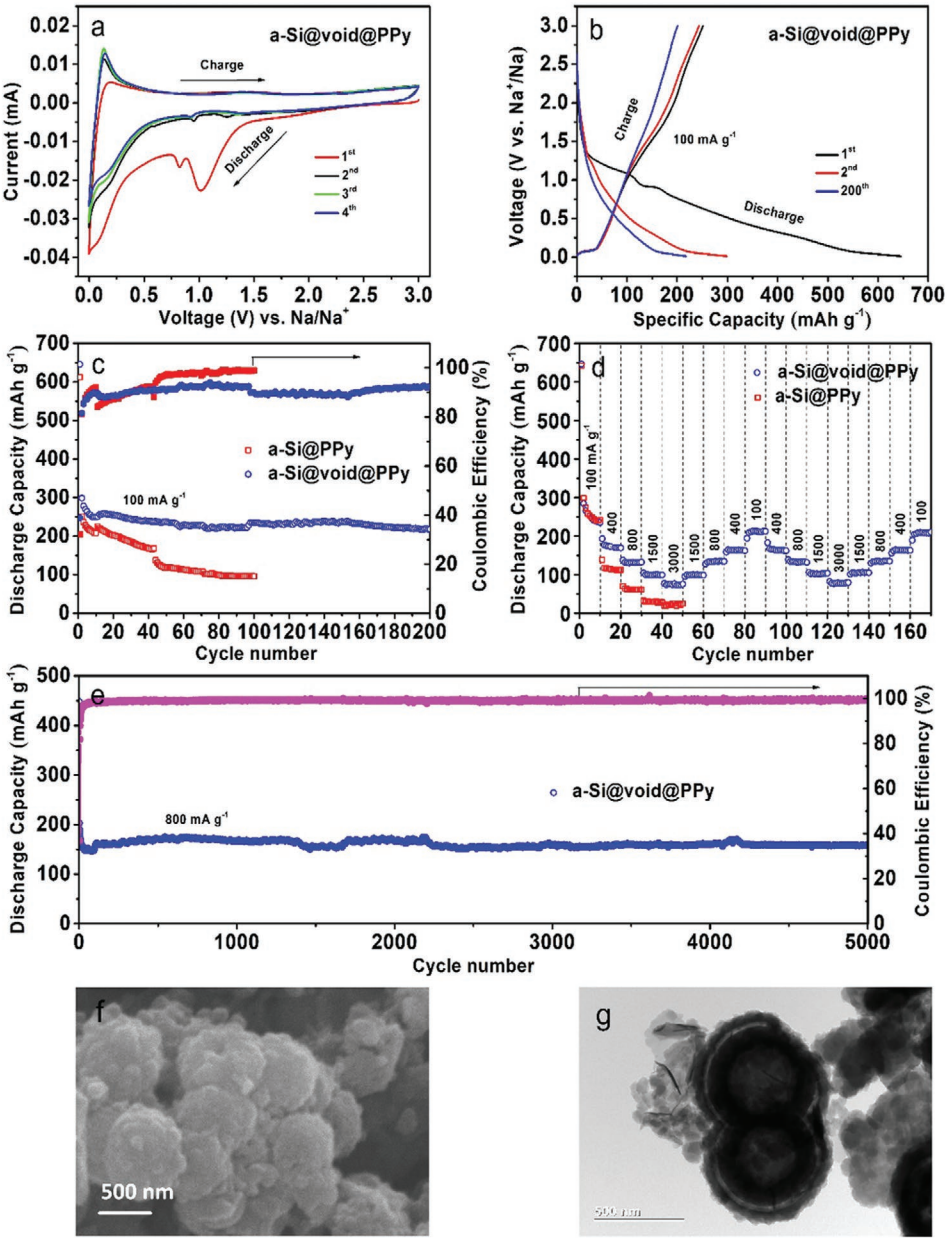

Figure 3. a) CV curves and b) galvanostatic charge-discharge plots of the a-Si@void@PPy composite. c) Cycling performance and CEs of the a-Si@void@PPy and a-Si@PPy composites at 100 mA g^{-1}. d) Rate capability of the a-Si@void@PPy and a-Si@PPy composites at a variety of current densities. e) Long-term cycling performance and CEs of the a-Si@void@PPy composite at 800 mA g^{-1}. f) SEM and g) TEM images of the a-Si@void@PPy composite after 50 cycles at different current densities from 100 to 3000 mA g^{-1}.

demonstrating that their capacity contribution to the a-Si@void@PPy composite was negligible. However, the a-Si@PPy composite presents capacity retention of only 38% at the 100th cycle in comparison with that at the second cycle. Therefore, the factors for the outstanding cycling stability of the a-Si@void@PPy composite are summarized as follows: 1) As a cushion, the porous hollow structure of a-Si is capable of partly providing the volume expansion and releasing the mechanical stress; 2) The yolk–shell structure is capable of offering inner void space, making swelling of a-Si take place freely in the process of cycling without ruining the outer shell; 3) The shell is capable of restraining the volume change and reducing the touch between the electrolyte and a-Si surface, generating a uniform SEI film.

The rate performance of the a-Si@void@PPy composite is displayed in Figure 3d. It delivers discharge capacities of 646.4, 193.5, 138.6, 105, and 77.5 mAh g^{-1} at the current densities of 100, 400, 800, 1500, and 3000 mA g^{-1}, respectively. When the current density is varied gradually from 3000 to 100 mA g^{-1}, the high capacity of 194.5 mAh g^{-1} is regained. Even after another cycling period, the capacities are still well maintained, indicating its repeatable rate capability. However, when the current density

of the a-Si@PPy composite is adjusted gradually from 100 to 3000 mA g^{-1}, a capacity of <20.0 mAh g^{-1} is obtained. Thus, the reasons for the superior rate performance of the a-Si@void@PPy composite are listed below: 1) The void space in the composite and porous hollow structure of a-Si are capable of making electrolyte soaked and shortening the transportation of Li^+ into the electrode; 2) The PPy shell is capable of improving the electrical conductivity of the electrode, proposing a valid electron transfer path from the a-Si to the current collector. To further confirm the structural stability, we carried out SEM and TEM analysis of the a-Si@void@PPy electrode after 50 cycles at various current densities from 100 to 3000 mA g^{-1}. It demonstrates that the morphology and structure of the a-Si@void@PPy composite are well retained (Figure 3f,g). Nevertheless, the a-Si@PPy electrode has a severe crack, and it is hard to distinguish the morphology after cycling (Figure S8, Supporting Information).

CV curves with multifarious scan rates from 0.1 to 1 mV s^{-1} were acquired for studying the sodium storage mechanism as well as the possible kinetics of the a-Si@void@PPy electrode (**Figure 4**a). All the CV curves have low polarized voltage with even shape, suggesting a rapid reaction kinetics process. It is widely known that the relationship of the current (i) and sweep rate (ν) is in accordance with a power law of $i = a\nu^b$ according to the log (i) versus log (ν) plots. When b nears 0.5, it implies a diffusion-controlled process occurred at the electrode while when b approaches 1.0, the sodium storage process is more surface-controlled.[21] Figure 4b shows that the b-values for cathodic/anodic peaks are quantitatively 0.571/0.728, respectively, indicating that the ion diffusion effect controls the electrochemical reactions. Furthermore, the capacitive capacity can be quantitatively evaluated by $i(V) = k_1\nu + k_2\nu^{1/2}$, where $i(V)$ means the current response at

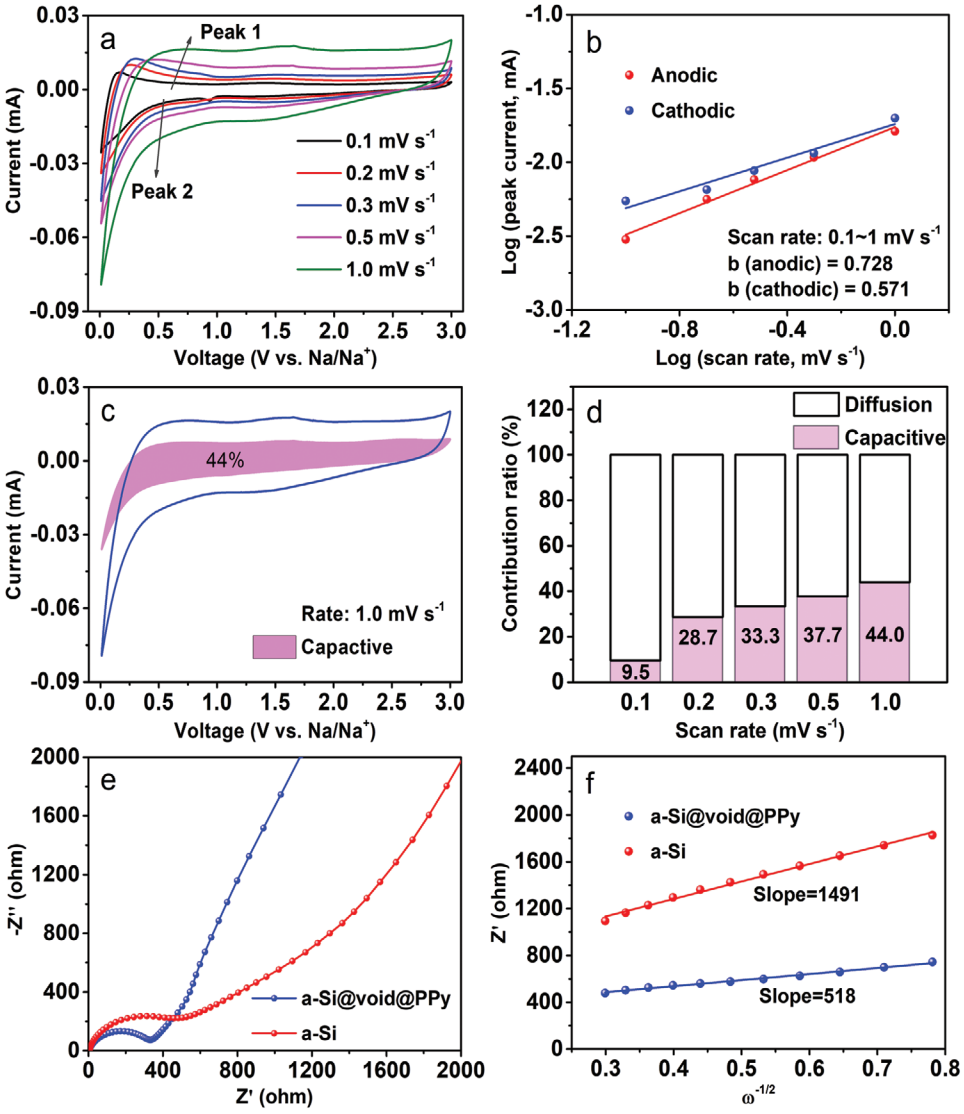

Figure 4. a) CV profiles of the a-Si@void@PPy composite from 0.1 to 1 mV s^{-1}. b) b-values for cathodic and anodic peaks. c) Separation of the capacitive and diffusion currents at 1.0 mV s^{-1}. d) Normalized contribution ratio of capacitive and diffusion-controlled capacities at different rates. e) Nyquist plots and corresponding fitted curves of the a-Si and a-Si@void@PPy electrodes after 50 cycles at a current density of 100 mA g^{-1}. f) Z′ as a function of the $\omega^{-1/2}$ plot in the low frequency range (the slope of fitting curves is the Warburg factor, σ_ω).

a fixed potential (V), k_1 and k_2 are tunable figures, and $k_1\nu$ and $k_2\nu^{1/2}$ mean the pseudocapacitive contribution and diffusion-controlled contribution, respectively.[22] Figure 4c indicates that the capacitive contribution at a scan rate of 1.0 mV s^{-1} for the a-Si@void@PPy electrode accounts for 44.0% of the total capacity. Figure 4d shows the contribution ratios of capacitive and diffusion behaviors from 0.1 to 1.0 mV s^{-1}. The results demonstrate that the capacitive contribution progressively increases with the improvement of the scan rate, meaning that high rates restrain the lithium diffusion process. The electrochemical impedance spectroscopy (EIS) measurements of the a-Si@void@PPy and a-Si electrodes were conducted after 50 cycles at a current density of 100 mA g^{-1}. The value of R_{ct} for a-Si@void@PPy (329 Ω) is remarkably lower than that of a-Si (523 Ω), as depicted in Figure 4e, which clearly manifests that the a-Si@void@PPy electrode undergoes a faster charge transfer process than the a-Si electrode. Furthermore, the diffusion coefficient of sodium ions can be calculated using the equation as follows:

$$D_{Na^+} = R^2 T^2 / \left(2A^2 n^4 F^4 C^2 \sigma_\omega^2\right) \quad (4)$$

From Figure 4f, the Warburg coefficients σ_ω of a-Si@void@PPy and a-Si after the 100th cycle are 518 and 1491 Ω $s^{-0.5}$, respectively, and according to Equation (4),[23] the D_{Na^+} is identified as 1.03×10^{-16} and 4.39×10^{-18} cm^2 s^{-1}, respectively, further demonstrating that a-Si@void@PPy possesses a higher diffusion coefficient of sodium ions.

To prove the superiority of the yolk-shell structure, the live sodiation processes of the a-Si@void@PPy and a-Si@PPy composites were explored through the in situ TEM. From the diagram in **Figure 5**a, the in situ electrochemical experiment setup includes Na/Na_2O coated on a tungsten (W) probe, and sample adhered on a gold (Au) rod. The automatically formed Na_2O on Na can act as a solid electrolyte. The technique lets us straightly study the structural evolution and stability during battery operation. The pictures captured from a video of the in situ sodiation of the a-Si@void@PPy composite (Video S1, Supporting Information) are shown in Figure 5b–d. It is observable that the a-Si hollow nanosphere is encapsulated inside a bigger PPy hollow nanosphere before sodiation (Figure 5b). Then, the volume of a-Si swells as Na^+ infiltrates into the PPy and alloys with a-Si. The a-Si@void@PPy composite is partially

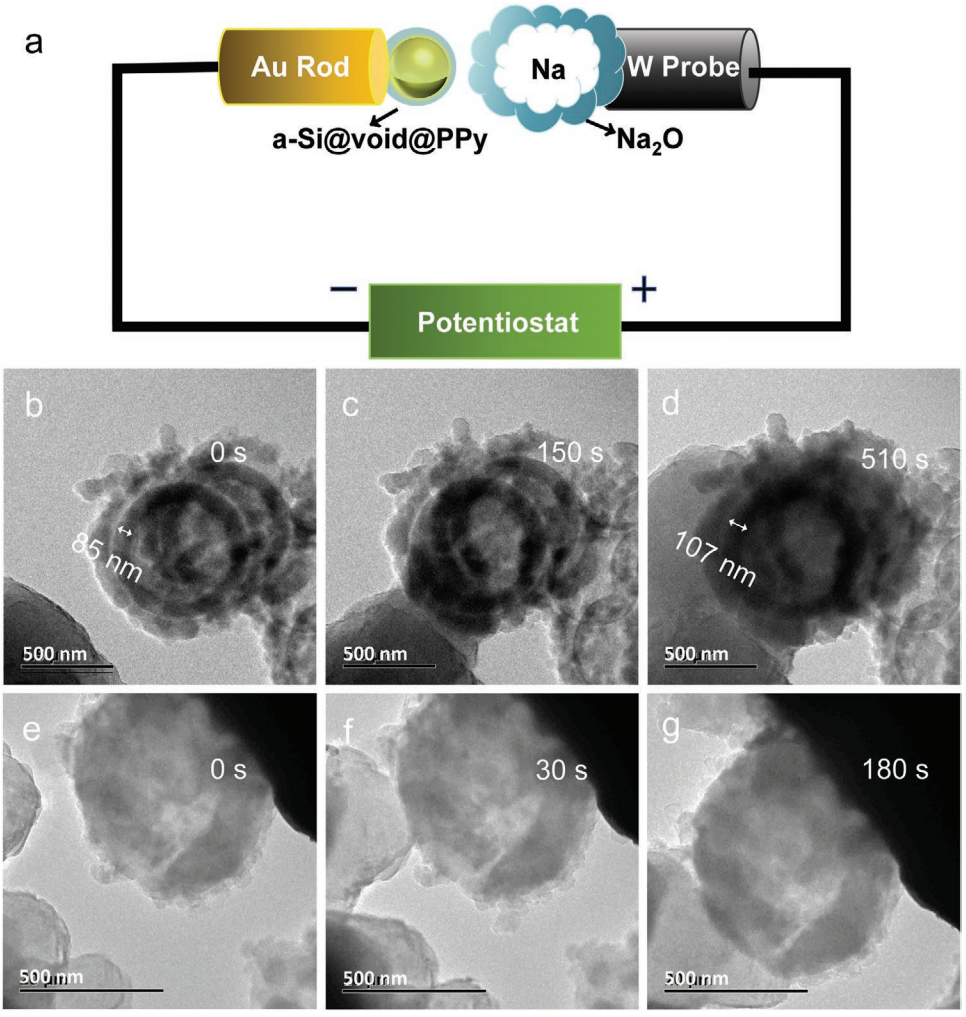

Figure 5. a) Diagram of the nanoscale electrochemical cell for in situ sodiation within the TEM. b–g) Time-lapse images of the sodiation of (b–d) a-Si@void@PPy and (e–g) a-Si@PPy composites.

sodiated after 150 s (Figure 5c). After 510 s, the overall structure will no longer change, manifesting that the composite is fully sodiated (Figure 5d). The outer radius and inner radius of the a-Si yolk are enlarged from 315/230 to 396/289 nm during the entire process, showing a 100% volume expansion. Moreover, no fracture of the PPy hollow nanospheres is viewed, benefiting from the structure offered moderate void space for the yolk to change freely without ruining the shell. For the a-Si@PPy composite, however, the PPy layer is slowly peeled off from the a-Si surface, and finally the whole structure is deformed, even appearing a crack (Figure 5e–g; Video S2, Supporting Information). Total observations demonstrate that the well-designed structure can effectively prevent the SIBs anode structure from varying and improve the cycle life consequently.

2.3. Theoretical Calculation

The void space is a highly significant factor that affects the electrochemical performance of a-Si anode. The superiorities of the yolk-shell structure were further verified by finite element simulation. Table S2 (Supporting Information) lists the Young's moduli and Poisson's ratios of Na, a-Si, $Na_{0.76}Si$, and PPy.[24–26] The geometric parameters of the initial shapes are shown in Table S3 (Supporting Information). The expansion of a-Si with thorough sodiation is presumed to be 114%. The a-Si and the PPy were discretized applying the brick element (C3D8R). Just one-fourth of the total structure was researched due to the symmetry (**Figure 6**). In the simulation, the maximum Mises stress on the PPy shell for the composite with 36 nm thickness of void space is ≈8.1 MPa (Figure 6d), which is lower than that (≈15.0 MPa) for the composite without void space (Figure 6b). Due to the tensile strength of the PPy shell can achieve 10.0 MPa,[27] the shell for the a-Si@void@PPy composite will still be unbroken after complete sodiation, whereas that for the a-Si@PPy composite will crack. In addition, when the maximum Mises stresses are equal to zero (Figure 6h) and the shell's fracture stress (10.0 MPa, Figure 6f), the thicknesses of void space are calculated to be 91 and 25 nm, respectively. Therefore, the range of reasonable values for the void space is between 25 and 91 nm. Under these conditions, the yolk–shell structure can not only enable the electrical contact between a-Si and PPy, but also prevent the PPy from destroying. The geometric parameters and the maximum contact stresses of

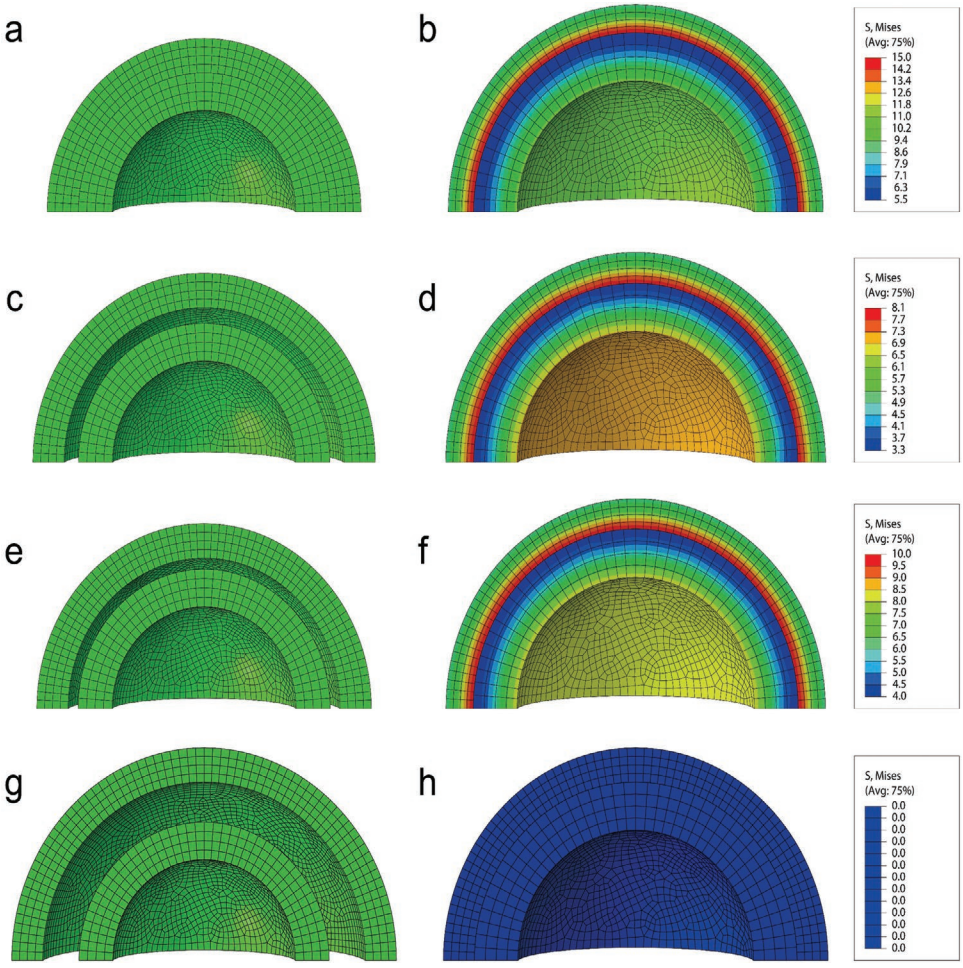

Figure 6. a) The initial shape and b) the deformed shape and stress distribution of a-Si@PPy composite. c) The initial shape and d) the deformed shape and stress distribution of a-Si@void@PPy composite. e) The initial shape and f) the deformed shape and stress distribution of composite with 25 nm thickness of void space. g) The initial shape and h) the deformed shape and stress distribution of composite with 91 nm thickness of void space.

the deformed shapes for the four models are summarized in Table S3 (Supporting Information).

3. Conclusion

In conclusion, a-Si@void@PPy composite has been successfully prepared through low-temperature sodiothermic reduction of $MHSiO_2$, ALD of alumina, in situ chemical polymerization of pyrrole, and dilute HCl etching. The resulting composite is designed with intriguing void space between a-Si core and pyrrole shell, thus delivering excellent rate performance, ultra-long cycle life, and large reversible capacities as an anode material for SIBs. The porous hollow structure of a-Si can partially provide the volume expansion and facilitate the electrolyte infusion and Li^+ transportation in the electrode. The PPy shell is capable of increasing the overall electrical conductivity of the electrode and decreasing the touch between the a-Si surface and electrolyte. The yolk–shell structure offers internal void space for self-accommodation of large volume variation of a-Si. The superiorities of the yolk–shell structure in the course of sodiation were verified by in situ TEM observation and FE simulation. This work not only supplies a new synthesis approach for the application of a-Si in other fields but also presents a new design strategy for the improvement of electrochemical properties of other alloy-type anode materials.

4. Experimental Section

Materials: Tetraethylorthosilicate (TEOS), ethanol, cetyltrimethylammonium bromide (CTAB), ammonia solution (25 wt%), hydrochloric acid solution (37 wt%), polyvinylpyrrolidone (PVP, Mw 1 300 000), pyrrole, and iron chloride hexahydrate were purchased from Sinopharm Chemical Reagent Co., Ltd. All the chemicals mentioned above were used as received.

Synthesis of $MHSiO_2$: The synthesis of $MHSiO_2$ was following a process presented in the literature. Normally, 0.15 g of CTAB was immersed in 80 ml of ethanol/H_2O solvent (volume ratio = 3:5) containing concentrated NH_4OH (1 ml, 25 wt%). TEOS was rapidly dropped into the above solution under vigorous agitation and hydrolyzed at 35 °C for 24 h. Subsequently, the white SiO_2 floccule was obtained after filtration and cleaned by absolute ethanol. The precipitation was soaked in deionized water (160 ml) at 90 °C for 48 h. After filtration, the sample was re-soaked in absolute ethanol (120 ml) containing concentrated HCl (240 µl, 37%) and stirred at 60 °C for 3 h to remove the CTAB.

Preparation of a-Si Hollow Nanospheres: In a glovebox, $MHSiO_2$ (0.1 g) and sodium (0.1 g) were poured into a glass tube, vacuum-sealed, and then placed in a muffle furnace at 450 °C for 100 min. The ramping rate was maintained at 1 °C min^{-1}. After breaking the glass tube, the product was immersed in absolute ethanol to remove a small amount of sodium and then soaked in dilute HCl to remove sodium oxides. The sample gained by filtration was transferred into a vacuum oven at 60 °C for 12 h to dry.

Fabrication of a-Si@void@PPy Composite: First, a-Si@Al_2O_3 core-shell nanospheres were prepared by the ALD technique using trimethylaluminum and water as precursors. The cycle number of ALD is 400 and the growth rate is 0.9 Å per cycle. The obtained nanospheres (0.05 g) and PVP (0.1535 g) were immersed in deionized water (100 ml) via ultrasonication, followed by stirring for 24 h. After centrifugation and clean with deionized water, the excess PVP was removed. The nanospheres containing PVP were redispersed in deionized water (100 ml). Second, pyrrole (50 µl) was added to the above solution with stirring for 6 h. $FeCl_3$ (0.45 g) was slowly added as an oxidizing agent and reacted at 0 °C for 24 h. The resulting black powder was centrifuged with ethanol to wash away residual $FeCl_3$ and heated at 60 °C for 12 h in a vacuum. After cleaning by 1 M HCl for 12 h, the alumina layer was removed and the final sample was collected.

Characterizations: The morphologies and structures of the obtained materials were researched employing a Hitachi SU1510 SEM and a JEOL JEM-2010F TEM. The composition and elemental mappings were investigated through EDX spectroscopy attached to the TEM instrument. The crystal phase was recorded by XRD through a Rigaku D/max-2550X diffractometer with Cu Kα radiation. The surface chemical state was examined through a Thermo Fisher Scientific ESCALAB spectrometer with Mg-Kα light source. The Raman spectrum was recorded via a Renishaw Invia Raman microscope with an excitation wavelength of 514 nm. The pore size distribution and surface area were determined using an ASAP 2010 M+C analyzer. TGA was performed by a Netzsch STA 449C thermoanalyzer in air.

Electrochemical Measurements: Sample, sodium carboxymethyl cellulose and distilled water were mixed for gaining a well-distributed slurry first. Subsequently, the mixture was drop-cast onto a Cu foil, followed by heating at 60 °C under vacuum for 12 h. The Cu foil was finally cut into small discs (12 mm). Coin cells (CR2032-type) were accomplished in a glovebox under an argon atmosphere using the prepared electrode as the working electrode, metal Na as the counter electrode, 1 M $NaClO_4$ in ethylene carbonate/diethyl carbonate (1:1, v/v) as the electrolyte, and glass fiber as the separator. Charge–discharge tests were investigated on a Neware CT-4008 battery test system. CV was performed on a VMP3 electrochemical workstation in the potential range 0.01–3 V.

In Situ TEM Examination: a-Si@void@PPy or a-Si@PPy composites were coated onto a gold rod as a working electrode, and metal sodium was adhered to a tungsten probe and acted as the sodium source and counter electrode. A naturally formed Na_2O layer on sodium served as the solid electrolyte. The nanobattery assembly was finished in a glovebox under an argon atmosphere. Then the hold (Hummingbird Scientific, USA) was rapidly moved into the TEM chamber. The Na/Na_2O contacted with the sample, and Na^+ was inserted into the sample using a constant –2 V potential. The sodiation processes were studied by a JEOL JEM-2010F TEM.

Simulation: FE analysis was carried out by the commercial software package ABAQUS (Simulia, Providence, RI, USA).

Supporting Information

Supporting Information is available from the Wiley Online Library or from the author.

Acknowledgements

F.H.D. and L.Z. contributed equally to this work. The authors are grateful to the Shanghai Municipal Education Commission (QD2019008) and the National Natural Science Foundation of China (52073170).

Conflict of Interest

The authors declare no conflict of interest.

Data Availability Statement

The data that support the findings of this study are available in the supplementary material of this article.

Keywords

amorphous Si-based anode material, finite element analysis, in situ transmission electron microscopy observation, sodiothermic reduction, sodium-ion batteries, yolk–shell structure

Received: November 17, 2021
Revised: December 21, 2021
Published online:

[1] N. Yabuuchi, K. Kubota, M. Dahbi, S. Komaba, *Chem. Rev.* **2014**, *114*, 11636.
[2] J. Qian, X. Wu, Y. Cao, X. Ai, H. Yang, *Angew. Chem., Int. Ed.* **2013**, *52*, 4633.
[3] F. H. Du, K. X. Wang, J. S. Chen, *J. Mater. Chem. A* **2016**, *4*, 32.
[4] F. H. Du, Y. Ni, Y. Wang, D. Wang, Q. Ge, S. Chen, H. Y. Yang, *ACS Nano* **2017**, *11*, 8628.
[5] F. H. Du, B. Li, W. Fu, Y. J. Xiong, K. X. Wang, J. S. Chen, *Adv. Mater.* **2014**, *26*, 6145.
[6] F. Legrain, O. I. Malyi, S. Manzhos, *Comput. Mater. Sci.* **2014**, *94*, 214.
[7] S. C. Jung, D. S. Jung, J. W. Choi, Y. K. Han, *J. Phys. Chem. Lett.* **2014**, *5*, 1283.
[8] S. Huang, L. Liu, Y. Zheng, Y. Wang, D. Kong, Y. Zhang, Y. Shi, L. Zhang, O. G. Schmidt, H. Y. Yang, *Adv. Mater.* **2018**, *30*, 1706637.
[9] Y. Han, N. Lin, T. Xu, T. Li, J. Tian, Y. Zhu, Y. Qian, *Nanoscale* **2018**, *10*, 3153.
[10] Q. Zhao, Y. Huang, X. Hu, *Electrochem. Commun.* **2016**, *70*, 8.
[11] M. K. Jangid, A. Vemulapally, F. J. Sonia, M. Aslam, A. Mukhopadhyay, *J. Electrochem. Soc.* **2017**, *164*, A2559.
[12] C. H. Lim, T. Y. Huang, P. S. Shao, J. H. Chien, Y. T. Weng, H. F. Huang, B. J. Hwang, N. L. Wu, *Electrochim. Acta* **2016**, *211*, 265.
[13] F. Cherif, I. B. Ahmed, A. Abderrahmane, S. Hamzaoui, *Mater. Sci.-Pol.* **2019**, *37*, 122.
[14] Z. Bao, M. R. Weatherspoon, S. Shian, Y. Cai, P. D. Graham, S. M. Allan, G. Ahmad, M. B. Dickerson, B. C. Church, Z. Kang, H. W. AbernathyIII, C. J. Summers, M. Liu, K. H. Sandhage, *Nature* **2007**, *446*, 172.
[15] H. Jia, P. Gao, J. Yang, J. Wang, Y. Nuli, Z. Yang, *Adv. Energy Mater.* **2011**, *1*, 1036.
[16] N. F. Mott, edited by P. G. Le Comber, J. Mort, Academic Press, New York **1973**.
[17] N. Liu, H. Wu, M. T. McDowell, Y. Yao, C. Wang, Y. Cui, *Nano Lett.* **2012**, *12*, 3315.
[18] B. Huang, X. Li, Y. Pei, S. Li, X. Cao, R. C. Masse, G. Cao, *Small* **2016**, *12*, 1945.
[19] R. Mo, D. Rooney, K. Sun, *iScience* **2018**, *9*, 521.
[20] E. Pollak, G. Salitra, V. Baranchugov, D. Aurbach, *J. Phys. Chem. C* **2007**, *111*, 11437.
[21] H. Wang, T. Yao, C. Li, L. Meng, Y. Cheng, *Chem. Eng. J.* **2020**, *397*, 125385.
[22] H. Zhang, W. Sun, X. Chen, Y. Wang, *ACS Nano* **2019**, *13*, 14252.
[23] S. Zhang, Y. Zeng, Z. Wang, J. Zhao, G. Dong, *Chem. Eng. J.* **2018**, *334*, 487.
[24] J. Guo, Z. Jia, *J. Power Sources* **2021**, *486*, 229371.
[25] M. Mortazavi, J. Deng, V. B. Shenoy, N. V. Medhekar, *J. Power Sources* **2013**, *225*, 207.
[26] G. M. Spinks, B. Xi, V. T. Truong, G. G. Wallace, *Synth. Met* **2005**, *151*, 85.
[27] K. S. U. Schirmer, D. Esrafilzadeh, B. C. Thompson, A. F. Quigley, R. M. I. Kapsa, G. G. Wallace, *J. Mater. Chem. B* **2016**, *4*, 1142.